# Hydraulic Fracture Diagnostics from Krauklis Wave Resonance and Tube Wave Reflections

**Chao Liang[1], Ossian O'Reilly[1,3], Eric M. Dunham[1,2], Dan Moos[4]**

[1] *Department of Geophysics, Stanford University, Stanford, California, USA. E-mail: chao2@stanford.edu, ooreilly@stanford.edu,edunham@stanford.edu*

[2] *Institute for Computational and Mathematical Engineering, Stanford University, Stanford, California, USA.*

[3] *Baker Hughes, Palo Alto, California, USA.*

[4] *formerly at Baker Hughes, Palo Alto, California, USA. E-mail: dbmoos1@earthlink.net*

(September 9, 2016)

Running head: **Fracture diagnostics with Krauklis waves and tube waves**



## ABSTRACT

Fluid-filled fractures support guided waves known as Krauklis waves. Resonance of Krauklis waves within fractures occurs at specific frequencies; these frequencies, and associated attenuation of the resonant modes, can be used to constrain fracture geometry. Here we use numerical simulations of wave propagation along fluid-filled fractures to quantify fracture resonance. The simulations involve solution of an approximation to the compressible Navier-Stokes equation for the viscous fluid in the fracture coupled to the elastic wave equation in the surrounding solid. Variable fracture aperture, narrow viscous boundary layers near the fracture walls, and additional attenuation from seismic radiation are accounted for in the simulations. We then demonstrate how tube waves within a wellbore can be used to excite Krauklis waves within fractures that are hydraulically connected to

the wellbore. The simulations provide the frequency-dependent hydraulic impedance of the fracture, which can then be used in a frequency-domain tube wave code to model tube wave reflection/transmission from fractures from a source in the wellbore or at the wellhead (e.g., water hammer from abrupt shut-in). Tube waves at the resonance frequencies of the fracture can be selectively amplified by proper tuning of the length of a sealed section of the wellbore containing the fracture. The overall methodology presented here provides a framework for determining hydraulic fracture properties via interpretation of tube wave data.

# INTRODUCTION

Hydraulic fracturing is widely used to increase the permeability of oil and gas reservoirs. This transformative technology has enabled production of vast shale oil and gas resources. While engineers now have optimal control of well trajectories, the geometry (length, height, and aperture) of hydraulic fractures is still poorly known, which poses a challenge for optimizing well completion. Monitoring hydraulic fracture growth is desirable for many reasons. Tracking the length of fractures ensures that multiple, subparallel fractures remain active, rather than shielding each other through elastic interactions. It might also be used to prevent fractures in nearby wells from intersecting one another. In addition, the ability to measure fracture geometry would facilitate estimates of the stimulated volume and could be used to help guide the delivery of proppant.

Due to their sensitivity to properties of the surrounding formation and fractures intersecting the wellbore, tube waves or water hammer propagating along the well are widely used for formation evaluation and fracture diagnostics (Paillet, 1980; Paillet and White, 1982; Holzhausen and Gooch, 1985a,b; Holzhausen and Egan, 1986; Tang and Cheng, 1989; Hornby et al., 1989; Paige et al., 1992, 1995; Kostek et al., 1998a,b; Patzek and De, 2000; Henry et al., 2002; Derov et al., 2009; Ionov, 2007; Ziatdinov et al., 2006; Wang et al., 2008; Mondal, 2010; Bakku et al., 2013; Carey et al., 2015; Livescu et al., 2016). Here we are specifically concerned with low frequency tube waves having wavelengths much greater than the wellbore radius. In this limit, tube waves propagate with minimal dispersion at a velocity slightly less than the fluid sound speed (Biot, 1952). Besides excitation from sources within the well or at the wellhead, tube waves can be generated by incident seismic waves from the surrounding medium (Beydoun et al., 1985; Schoenberg, 1986; Ionov and

Maximov, 1996; Bakku et al., 2013) and by sources within hydraulic fractures (Krauklis and Krauklis, 1998; Ionov, 2007; Derov et al., 2009). Furthermore, tube waves incident on a fracture in hydraulic connection to the wellbore will reflect and transmit from the fracture, with frequency-dependent reflection/transmission coefficients. As described in more detail below, these reflected and transmitted tube waves carry information about fracture geometry.

A closely related concept is that of hydraulic impedance testing (Holzhausen and Gooch, 1985a), initially developed to estimate the geometry of axial fractures (fractures in the plane of the wellbore). This method, utilizing very low frequency tube waves or water hammer signals, was validated through laboratory experiments (Paige et al., 1992) and applied to multiple field datasets (Holzhausen and Egan, 1986; Paige et al., 1995; Patzek and De, 2000; Mondal, 2010; Carey et al., 2015). The method is typically presented using the well-known correspondence between hydraulics and electrical circuits. The fracture consists of a series connection of resistance (energy loss through viscous dissipation), capacitance (energy stored in elastic deformation of the solid and compression/expansion of the fluid), and inertance (kinetic energy of the fluid), which can be combined into a complex-valued hydraulic impedance of the fracture. The hydraulic impedance is then related to the geometry of the fractures (Holzhausen and Gooch, 1985a; Paige et al., 1992; Carey et al., 2015). However, this method, at least as presented in the literature thus far, assumes quasi-static fracture response when relating (spatially uniform) pressure in the fracture to fracture volume. This assumption is valid only for extremely low frequencies, and neglects valuable information at higher frequencies where there exists the possibility of resonant fracture response associated with waves propagating within the fracture. The treatment of dissipation from fluid viscosity is similarly overly simplistic.

Thus a more rigorous treatment of the fracture response is required, motivating a more nuanced description of the dynamics of fluid flow within the fracture and of its coupling to the surrounding elastic medium over a broader ranger of frequencies. The key concept here is a particular type of guided wave that propagates along fluid-filled cracks. These waves, known as crack waves or Krauklis waves, have been studied extensively in the context of the oil and gas industry, volcano seismology, and other fields (Krauklis, 1962; Paillet and White, 1982; Chouet, 1986; Ferrazzini and Aki, 1987; Korneev, 2008; Yamamoto and Kawakatsu, 2008; Korneev, 2010; Dunham and Ogden, 2012; Lipovsky and Dunham, 2015; Nikitin et al., 2016). At the frequencies of interest here (∼1–1000 Hz), they are anomalously dispersed waves of opening and closing that propagate along fractures at speeds ∼10–1000 m/s. Experimental studies have confirmed the existence and propagation characteristics of these waves (Tang and Cheng, 1988; Nakagawa, 2013; Shih and Frehner, 2015; Nakagawa et al., 2016). Counter-propagating pairs of Krauklis waves form standing waves (eigenmodes) of fluid-filled cracks, and the resonance frequencies and decay rates of these modes are sensitive to both fracture length and aperture. Krauklis waves are thought to be responsible for the long period and very long period seismicity at active volcanoes (Aki et al., 1977; Chouet, 1988) and have been suggested as a possible explanation for harmonic seismic signals recorded during hydraulic fracturing treatments (Ferrazzini and Aki, 1987; Tary et al., 2014). Most studies of Krauklis waves have been analytical or semi-analytical, with a major focus on deriving dispersion relations for waves in infinitely long fluid layers of uniform width. A notable exception is the work of Frehner and Schmalholz (2010) and Frehner (2013), in which finite elements in two dimensions were used to study Krauklis waves in finite-length fractures with variable aperture. Using a numerical approach provides a means to investigate the reflection and scattering of Krauklis waves at fracture tips (Frehner and

Schmalholz, 2010) and the excitation of Krauklis waves by incident seismic waves (Frehner, 2013). However, these studies did not consider the interaction between the Krauklis waves and tube waves, which is a central focus of our study.

Mathieu and Toksoz (1984) were the first to pose the mathematical problem of tube wave reflection/transmission across a fracture in terms of the fracture impedance, defined in the frequency domain as

$$Z_f(\omega) = \frac{\hat{p}_f(\omega)}{\hat{u}(\omega)}, \tag{1}$$

where $\hat{p}_f(\omega)$ and $\hat{u}(\omega)$ are the Fourier transforms of pressure and the cross-sectionally averaged fluid velocity into the fracture, both evaluated at the fracture mouth. The Fourier transform of some function $u(t)$ is defined as

$$\hat{u}(\omega) = \int_{-\infty}^{\infty} u(t) e^{i\omega t} dt. \tag{2}$$

Mathieu and Toksoz (1984) treated the fracture as a infinite fluid layer or a permeable porous layer with fluid flow described by Darcy's law. The fracture impedance built on Darcy's law was then replaced with analytic solutions based on the dispersion relation for acoustic waves in an inviscid (Hornby et al., 1989) or viscous (Tang and Cheng, 1989) fluid layer bounded by rigid fracture walls. Later studies established that elasticity of the fracture wall rock significantly changes the reflection and transmission across a fracture (Tang, 1990; Kostek et al., 1998a,b). The arrival time and amplitude of reflected tube waves can be used to infer the location and effective aperture of fractures (Medlin and Schmitt, 1994). However, most of these models assume infinite fracture length, as is well justified (Hornby et al., 1989) for the high frequencies ($\sim$1 kHz) that were the focus of these studies. By focusing instead on lower frequencies (<100 Hz) and considering Krauklis waves reflected from the fracture tip, Henry et al. (2002) and Henry (2005) argued that reflection/transmission of tube waves is

affected by the resonance of the fracture, and consequently provides sensitivity to fracture length.

One approach to account for the finite extent of the fracture is to use the dispersion relation for harmonic Krauklis waves to determine the eigenmodes of a circular disk-shaped fracture of uniform aperture with a zero radial velocity boundary condition at the edge of the disk (Hornby et al., 1989; Henry et al., 2002; Henry, 2005; Ziatdinov et al., 2006; Derov et al., 2009). This treatment fails to account for the decreased aperture near the fracture edge, which both decreases the Krauklis wave phase velocity and increases viscous dissipation. It furthermore implicitly assumes perfect reflection from the fracture edge, thereby neglecting attenuation from seismic wave radiation. Recent studies have established the importance of this attenuation mechanism (Frehner and Schmalholz, 2010; Frehner, 2013).

In this work, we examine how Krauklis waves propagating in fluid-filled fractures, as well as tube wave interactions with fractures, can be used to infer fracture geometry. Figure 1 shows the system. The overall problem is to determine the response of the coupled fracture-wellbore system to excitation at the wellhead, within the wellbore, or at the fracture mouth. Other excitation mechanisms, including sources in the fracture or incident seismic waves from some external source in the solid (e.g., microseismic events or active sources), are not considered here. The fracture and wellbore are coupled in several ways, the most important of which is through the direct fluid contact at the fracture mouth. Pressure changes at this junction, for instance due to tube waves propagating along the wellbore, will excite Krauklis waves in the fracture. Similarly, fluid can be exchanged between the wellbore and fracture. Other interactions, such as through elastic deformation of the solid surrounding the wellbore and fracture, are neglected in our modeling approach.

By making this approximation, and by further assuming that all perturbations are sufficiently small so as to justify linearization, the response of the coupled fracture-wellbore system can be obtained in two steps (Mathieu and Toksoz, 1984; Hornby et al., 1989; Kostek et al., 1998a; Henry, 2005). In the first step, we determine the response of the fracture, in isolation from the wellbore, to excitation at the fracture mouth. Specifically, we calculate the (frequency-dependent) hydraulic impedance of the fracture, as defined in equation 1, using high-resolution finite difference simulations of the dynamic response of a fluid-filled fracture embedded in a deformable elastic medium. This provides a rigorous treatment of viscous dissipation and seismic radiation along finite-length fractures with possibly complex geometries, including variable aperture. The numerical solutions are compared to semi-analytic solutions based on dispersion relations for harmonic waves propagating along an infinitely long fluid layer of uniform width. In the second step, we solve the tube wave problem in the frequency domain, where the fracture response is captured through the fracture impedance, and then convert to the time domain by inverting the Fourier transforms. The fracture response, as embodied by the fracture impedance, features multiple resonance peaks associated with the eigenmodes of the fracture. The frequencies and attenuation properties of these modes are sensitive to both fracture length and aperture. These resonances furthermore make the tube wave reflection/transmission coefficients dependent on frequency, with maximum reflection at the resonance frequencies of the fracture. We close by presenting synthetic pressure seismograms for tube waves within the wellbore, along with a demonstration of the sensitivity of these signals to fracture geometry.

# FLUID-FILLED FRACTURES

## Fluid governing equations and numerical simulations of fluid-filled fractures

The first step in the solution procedure outlined above is to determine the hydraulic impedance of the fracture. In fact, we find it more convenient to work with a nondimensional quantity proportional to the reciprocal of the fracture impedance, which we refer to as the fracture transfer function, $F(\omega)$. While the fracture impedance diverges in the low frequency limit, the fracture transfer function goes to zero in a manner that captures the quasi-static fracture response utilized in the original work on hydraulic impedance testing.

The fluid-filled fracture system is described by the elastic wave equation, governing displacements of the solid, and the compressible Navier–Stokes equation for the viscous fluid in the fracture. In this work, we utilize a linearized, approximate version of the Navier–Stokes equation that retains only the minimum set of terms required to properly capture the low frequency response of the fluid (Lipovsky and Dunham, 2015). By low frequency we mean $\omega w_0/c_0 \ll 1$, where $\omega$ is the angular frequency, $w_0$ is the crack aperture or width (the two terms are used interchangeably hereafter), and $c_0$ is the fluid sound speed. For $w_0 \sim 1$ mm and $c_0 \sim 10^3$ m/s, frequencies must be smaller than about 1 MHz. This is hardly a restriction since fracture resonance frequencies are typically well below ∼100 Hz. Derivation of the governing equations and details of numerical treatment (using a provably stable, high-order-accurate finite difference discretization) are discussed in Lipovsky and Dunham (2015), OReilly et al. (2014) and O'Reilly, Dunham, and Nordström, manuscript in preparation, 2016. Here, we explain the geometry of our simulations and then briefly review the fluid governing equations within the fracture to facilitate the later discussion of

Krauklis waves and the fracture transfer function.

While solution to the 3D problem is required to quantify how the fracture transfer function depends on fracture length, height, and width, in this preliminary study we instead utilize a 2D plane strain model (effectively assuming infinite fracture height). We anticipate this 2D model will provide a reasonable description of axisymmetric fractures, like the one illustrated in Figure 1, though some differences should be expected from the differing nature of plane waves and axisymmetric waves. However, the procedure for utilizing the fracture transfer function, obtained from numerical simulations, to solve the coupled wellbore-fracture problem, is completely general, as are the overall qualitative results concerning matched resonance that are discussed in the context of tube wave interactions with fractures. Finally, when fracture transfer functions from 3D simulations are available, the coupling solution procedure can be used with no additional modifications.

Returning to the 2D plane strain problem, let $x$ be the distance along the fracture and $y$ the distance perpendicular to the fracture; the origin is placed at the fracture mouth, where we will later couple the fracture to a wellbore. We utilize an approximation similar in many respects to the widely used lubrication approximation for thin viscous layers (Batchelor, 2000), though we retain terms describing both fluid inertia and compressibility. In the low frequency limit ($\omega w_0/c_0 \ll 1$), the $y$-momentum balance establishes uniformity of pressure across the width of the fracture (Ferrazzini and Aki, 1987; Korneev, 2008; Lipovsky and Dunham, 2015). The linearized $x$-momentum balance is

$$\rho \frac{\partial v}{\partial t} + \frac{\partial p}{\partial x} = \mu \frac{\partial^2 v}{\partial y^2}, \tag{3}$$

where $v(x, y, t)$ is the particle velocity in the $x$-direction, $p(x, t)$ is the pressure, and $\rho$ and $\mu$ are the fluid density and dynamic viscosity, respectively. We have retained only the viscous

term corresponding to shear along planes parallel to $y = 0$; scaling arguments show that other viscous terms are negligible in comparison for this class of problems (Lipovsky and Dunham, 2015). The initial and perturbed fracture widths are defined as

$$w_0(x) = w_0^+(x) - w_0^+(x), \tag{4}$$

$$w(x,t) = w^+(x,t) - w^-(x,t). \tag{5}$$

Note that $w_0$ refers to the full width, whereas some previous work (Lipovsky and Dunham, 2015) used this to refer to half-width. Combining the linearized fluid mass balance with a linearized equation of state, we obtain

$$\frac{1}{K}\frac{\partial p}{\partial t} + \frac{1}{w_0}\frac{\partial w}{\partial t} = -\frac{1}{w_0}\frac{\partial\left(u w_0\right)}{\partial x}, \tag{6}$$

where

$$u(x,t) = \frac{1}{w_0(x)}\int_{w_0^-(x)}^{w_0^+(x)} v(x,y,t)dy \tag{7}$$

is the $x$-velocity averaged over the fracture width and $K$ is the fluid bulk modulus. The fluid sound speed is $c_0 = \sqrt{K/\rho}$. Accumulation/loss of fluid mass at some location in the fracture can be accommodated by either compressing/expanding the fluid (the first term on the left-hand side of equation 6) or opening/closing the fracture walls (the second term on the left-hand side of equation 6). The latter is the dominant process at the low frequencies of interest in this study.

Coupling between the fluid and solid requires balancing tractions and enforcing continuity of normal and tangential particle velocity on the fracture walls (i.e., the kinematic and no-slip conditions). At the fracture mouth, pressure is prescribed; zero velocity is prescribed at the fracture tip. At outer boundaries of the solid domain, absorbing boundary conditions are used to suppress artificial reflections. The computational domain in both directions is

12 times the length of the fracture so as to fully capture the quasi-static displacements in the solid and to further minimize boundary reflections.

Spatial variations in fracture width are captured through $w_0(x)$. A uniformly pressurized fracture in an infinite medium has an elliptical opening profile, $w_0(x) \propto \sqrt{L^2 - x^2}$, and a stress singularity at the fracture tips. Here we utilize a related solution for $w_0(x)$ in which closure at the tip occurs in a more gradual manner so as to remove that singularity. In particular, we use expressions for $w_0(x)$ from a cohesive zone model (Chen and Knopoff, 1986), appropriately modified from antiplane shear to plane strain by replacement of shear modulus $G$ with $G^* = G/(1-\nu)$ where $\nu$ is Poisson's ratio. The cohesive zone region is approximately 25% of the fracture length. In addition, we blunt the fracture tip so that it has finite width (usually a small fraction of the maximum width at the fracture mouth, unless otherwise indicated).

Figure 2 shows snapshots of the numerical simulation of Krauklis waves propagating along a fluid-filled fracture. For this example only, we add to $w_0(x)$ a band-limited self-similar fractal roughness, as in Dunham et al. (2011) with amplitude-to-wavelength ratio $10^{-2}$, similar to what is observed for natural fracture surfaces and faults (Power and Tullis, 1991; Candela et al., 2012). Material properties used in this and other simulations are given in Table 1. The fracture opens in regions of converging fluid flow and contracts where flow diverges. Krauklis waves with different wavelengths separate as they propagate along the fracture due to dispersion. Krauklis waves arise from the combined effects of fluid inertia and the restoring force from fracture wall elasticity. Since the elastic wall is more compliant at longer wavelengths, all else being equal, long wavelength waves experience smaller restoring forces and hence propagate more slowly. Elastic waves in the solid are excited both at the fracture mouth and along the fracture due to inertia of the solid during

Krauklis wave reflection from the fracture tip and fracture mouth. Note that elastic waves propagate nearly an order of magnitude faster than Krauklis waves; this is evident in panel (a). As seen in Figure 2 insets, viscous effects are primarily restricted to narrow boundary layers near the fracture walls and there can even be flow reversals and nonmonotonic velocity profiles. The decreased width near the fracture tip decelerates Krauklis waves and enhances viscous dissipation in the near-tip region. After being reflected multiple times, pairs of counter-propagating Krauklis waves form standing waves along the fracture, which set the fluid-filled fracture into resonance. Shorter period modes are damped out first, by both viscous dissipation and seismic radiation, leaving long period modes with wavelengths of order the fracture length. The frequency and decay rate, or attenuation, of these resonant modes is captured by the location and width of spectral peaks in the fracture transfer function, as we demonstrate shortly.



## Krauklis waves

However, before discussing the fracture transfer function, we review some key properties of Krauklis waves. This is most easily done in the context of an infinitely long fracture or fluid layer (with constant initial width $w_0$) between identical elastic half-spaces. Seeking $e^{i(kx-\omega t)}$ solutions to the governing equations, and neglecting inertia of the solid (which is negligible for Krauklis waves at the low frequencies of interest to us), leads to the dispersion relation (Lipovsky and Dunham, 2015)

$$D_K(k,\omega) = \left(\frac{\tan\xi}{\xi} - 1\right)\left(\frac{c_0 k}{\omega}\right)^2 + 1 + \frac{2K}{G^* k w_0} = 0, \tag{8}$$

where $\xi = \sqrt{-i w_0^2 \omega / 4\nu}$, $\nu = \mu/\rho$ is the fluid kinematic viscosity, $k$ is the wave number, and $\omega$ is the angular frequency. Using the full linearized Navier-Stokes equation for the fluid and

retaining inertia in the solid gives rises to a more complex dispersion relation (Ferrazzini and Aki, 1987; Korneev, 2008) that has both fundamental and higher mode solutions. In contrast, our approximate fluid model only captures the fundamental mode. However, the higher modes exist only above specific cut-off frequencies that are well outside the frequency range of interest. Here, we first discuss solutions to equation 8 for real $\omega$ and complex $k$. Spatial attenuation of the modes is quantified by

$$\frac{1}{2Q} = \frac{\operatorname{Im} k}{\operatorname{Re} k}, \tag{9}$$

where $Q$ is the quality factor, approximately the number of spatial oscillations required for appreciable decay of amplitude. Plots of phase velocity and attenuation are presented in Figure 3.

At high frequency (but still sufficiently low frequency as to justify the $\omega w_0/c_0 \ll 1$ approximation), the phase velocity approaches the fluid sound speed because the fracture walls are effectively rigid relative to the compressibility of the fluid. At frequencies below

$$f_{el} = \frac{\omega_{el}}{2\pi} = \frac{K c_0}{\pi G^* w_0}, \tag{10}$$

elastic wall deformation becomes appreciable. This additional compliance leads to reduced phase velocity, given approximately as (Krauklis, 1962)

$$c \approx \left( \frac{G^* w_0 \omega}{2\rho} \right)^{1/3}. \tag{11}$$

Lower frequency waves propagate slower than higher frequency waves because the elastic walls are more compliant at longer wavelengths. Viscous dissipation is confined to thin boundary layers around the fracture walls.

At even lower frequencies, below

$$f_{vis} = \frac{\omega_{vis}}{2\pi} = \frac{2\mu}{\pi \rho w_0^2}, \tag{12}$$

viscous effects are felt across the entire width of the fluid layer and the velocity $v$ approaches the well-known parabolic Poiseuille flow profile. Viscous dissipation is sufficiently severe as to damp out waves over only a few cycles of oscillation; in addition, phase velocity decreases below that given in equation 11.

An important consequence of dissipation, from both viscous effects and elastic wave radiation, is that Krauklis wave resonance will only occur in sufficiently short fractures. We can gain deeper insight by plotting the phase velocity and attenuation of Krauklis waves for real wavelength $\lambda$ and complex frequency in Figure 3c and d, which correspond to standing waves formed by pairs of counter-propagating Krauklis waves. The temporal attenuation is quantified by

$$\frac{1}{2Q} = \frac{\operatorname{Im}\omega}{\operatorname{Re}\omega}, \tag{13}$$

for temporal quality factor $Q$. When the wavelength exceeds a cutoff wavelength (Lipovsky and Dunham, 2015),

$$\lambda_c = 2\pi \left( \frac{60\mu^2}{G^* \rho w_0^5} \right)^{-1/3}, \tag{14}$$

the phase velocity drops to zero and temporal attenuation diverges. This expression, corresponding to the dashed lines in Figure 3c and d, provides a crude estimate of the maximum length of fractures that can exhibit resonant oscillations. However, it is essential to account for additional dissipation that occurs from the decreased width near the fracture tip, and this is best done numerically. We therefore quantify the detectability limits of fractures, using our 2D plane strain simulations, in a later section.

## Fracture transfer function

Now we turn our attention to finite-length fractures. Our objective is to quantify the response of the fracture to forcing at the fracture mouth, where the fracture connects to the wellbore. This is done through the dimensionless fracture transfer function $F(\omega)$ that relates pressure $p(0,t)$ and width-averaged velocity $u(0,t)$ at the fracture mouth:

$$\hat{u}(0,\omega) = \frac{F(\omega)}{\rho c_0}\hat{p}(0,\omega), \tag{15}$$

where $\hat{u}(0,\omega)$ and $\hat{p}(0,\omega)$ are the Fourier transform of width-averaged velocity and pressure, respectively. The fracture transfer function is related to the more commonly used fracture impedance $Z_f(\omega)$ defined in equation 1 by

$$F(\omega) = \frac{\rho c_0}{Z_f(\omega)}. \tag{16}$$

We have nondimensionalized $F(\omega)$ using the fluid acoustic impedance $\rho c_0$, such that $F(\omega) = 1$ for an infinitely long layer of inviscid fluid between parallel, rigid walls.

To calculate the fracture transfer function, numerical simulations such as that in Figure 2 are performed by imposing the pressure at the fracture mouth, $p(0,t)$, and measuring the resulting width-averaged velocity at the fracture mouth, $u(0,t)$. Figure 4 illustrates the sensitivity of $u(0,t)$ to the fracture geometry, given the same chirp input $p(0,t)$.

Then $p(0,t)$ and $u(0,t)$ are Fourier transformed and the fracture transfer function is calculated using equation 15. An example is shown in Figure 5. Figure 6 compares the amplitude of the transfer function, $|F|$, for fractures of different lengths and widths. The transfer functions exhibit multiple spectral peaks, corresponding to the resonant modes of the fracture (with a constant pressure boundary condition at the fracture mouth). These peaks are finite because of dissipation from both viscosity and seismic radiation. Longer

and narrower fractures have lower resonance frequencies, which is due to higher compliance and slower Krauklis wave phase velocities.

We next examine the asymptotic behavior of the fracture transfer function at low frequency, which facilitates comparison with quasi-static fracture models that have been widely used in the literature on hydraulic impedance testing and fracture diagnostics using water hammer signals (Holzhausen and Gooch, 1985a,b; Holzhausen and Egan, 1986; Paige et al., 1995; Mondal, 2010; Carey et al., 2015). By low frequency we mean $\omega \ll c(\omega)/L$, where $c(\omega)$ is the Krauklis wave phase velocity and $L$ is the fracture length. Using equation 11 for $c(\omega)$, the low frequency condition is $\omega \ll (G^* w_0 L^3/2\rho)^{1/2}$ or $\omega/2\pi \ll 15$ Hz for $L \sim 1$ m and $w_0 \sim 1$ mm. The low frequency condition results in effectively uniform pressure across the length of the crack (at least when viscous pressure losses can be neglected) and the fracture response can be described by a much simpler model. The global mass balance for the fracture, within the context of our linearization, is

$$w_0 u(0,t) \approx \frac{d}{dt}\int_0^L w(x,t)dx, \tag{17}$$

where we have assumed that the fluid is effectively incompressible at these low frequencies, such that inflow of fluid (the left-hand side) is balanced by changes in width (the right-hand side). Given that the fracture is very thin and approximately planar, the change in opening is then related to the pressure change using the well-known solution for a plane strain mode I crack in an infinite medium (Lawn, 1993). The result is

$$u(0,t) \approx \frac{\pi L^2}{4 w_0 G^*}\frac{dp}{dt} \tag{18}$$

It follows, upon Fourier transforming equation 18 and using equation 15, that

$$F(\omega) \approx \frac{-i\pi L^2 \rho c_0}{4 G^* w_0}\omega \quad \text{as} \quad \omega \to 0. \tag{19}$$

This asymptotic behavior is essentially the same as that quantified by Holzhausen and Gooch (1985a) as the fracture capacitance, though our result is for the 2D plane strain case to permit comparison to our simulations.

The low frequency asymptotes (equation 19) are plotted as dashed lines in Figures 5a (inset) and 6, verifying that our numerical simulations accurately capture the quasi-static response. However, this asymptotic behavior only applies in the extreme low frequency limit (far below the first resonance frequency) and deviates substantially from the actual response at higher frequencies. The traditional hydraulic impedance testing method (Holzhausen and Gooch, 1985a; Holzhausen and Egan, 1986) thus leaves the vast spectrum at higher frequencies unexplored.

We also derive an approximate analytical solution to the transfer function based on the dispersion relation (rather than using simulations). This dispersion-based approach has been utilized in several studies (Hornby et al., 1989; Kostek et al., 1998a; Henry, 2005; Derov et al., 2009) and it is illustrative to compare it to the more rigorous simulation-based solution. The solution, derived in appendix A, assumes uniform width and imposes a zero velocity boundary condition at the fracture tip. The resulting fracture transfer function is

$$F(\omega) = \frac{-ik(\omega)c_0 \tan\left[k(\omega)L\right]}{\omega}, \tag{20}$$

where $k(\omega)$ is the complex wavenumber obtained by solving the dispersion equation 8 for real angular frequency $\omega$.

Our numerical simulations permit exploration of how the decreased width near the fracture tip alters the fracture response, relative to more idealized models based on dispersion (equation 20) that assume tabular (uniform width) fractures. Figure 7 compares transfer functions for 1-m-long fractures with the same width (2 mm) at the fracture mouth but

different profiles near the tip. These range from a tabular fracture to ones in which the width at the tip is decreased to only 1/50 of the maximum width. As the fracture tip width is reduced, both the resonance frequencies and the fracture transfer function amplitude at resonance peaks are shifted to lower values. This is due to higher viscous dissipation and slower Krauklis wave phase velocity for narrower fractures. Differences are most pronounced at higher frequencies and for higher resonant modes. This finding highlights the importance of accounting for the near-tip geometry when utilizing high frequency data to determine fracture geometry. The tabular or flat fracture model (equation 20) can lead to substantial errors; in this example, there is about 20% error in the fundamental frequency and 100% error in the amplitude of the fundamental mode spectral peak.

## Fracture geometry inference and detectability limits

As evidenced by Figures 4–7, the fracture response, as embodied by the fracture transfer function, is sensitive to fracture geometry (both length and width). We now consider the inverse problem, that is, determining the fracture geometry from properties of the resonant modes of the fracture. Lipovsky and Dunham (2015), building on work by Korneev (2008) and Tary et al. (2014), showed how measurements of both resonance frequencies and attenuation or decay rates associated with resonant modes could be used to uniquely determine both length and width. Their work utilized dispersion relations derived for harmonic waves in an infinitely long fluid layer, and we have seen, in Figure 7, some notable discrepancies as compared to our numerical simulations of finite-length fractures. We thus revisit this problem, focusing in particular on detectability limits.

As the fracture length grows, the resonance wavelengths increase and eventually reach

a cutoff limit, beyond which the temporal attenuation diverges (Figure 3d). This provides the most optimistic estimate of fracture detectability using resonance; noise in real measurements will further limit detectability.

Figure 8a provides a graphical method for estimating fracture geometry from measurements of the frequency and temporal quality factor $Q$ of the fundamental mode. This is similar to Figures 6–8 in Lipovsky and Dunham (2015) but here the fundamental mode properties are determined from transfer functions from numerical simulations using the tapered fracture shape shown in Figure 6a. Specifically, $Q = f_0/\Delta f$ for fundamental frequency $f_0$ and $\Delta f$ the full width at half of the maximum amplitude in a plot of $|F|$ (e.g., Figure 6b). We also provide, in Figure 8b and c, a comparison between our numerical results (for tapered width) and predictions based on the dispersion relation (for uniform width). Note that the dispersion solutions are calculated for zero velocity at the fracture tip and constant pressure at the fracture mouth, whereas Lipovsky and Dunham (2015) assumed zero velocity at both tips. Viscous dissipation is underestimated using the dispersion-based approach, which ignores the narrow region near the fracture tip. There are also differences in resonance frequency; the finite-length fractures in our numerical simulations are stiffer, and hence resonate at higher frequencies, than suggested by the dispersion-based method.

We finish this section by noting that quantitative results in Figure 8 are specific to the 2D plane strain problem. We anticipate that an axisymmetric (penny-shaped) fracture would have a similar response, but caution that these results are unlikely to apply to 3D fractures when the length greatly exceeds the height. That case, which is of great relevance to the oil and gas industry, warrants study using 3D numerical simulations.

# TUBE WAVE INTERACTION WITH FLUID-FILLED FRACTURES

Having focused on the fracture response in the previous sections, we now return to the overall problem of determining the response of the coupled wellbore-fracture system. We present a simple model for low frequency tube waves and derive reflection/transmission coefficients that quantify tube wave interaction with a fracture intersecting the wellbore. We then examine the system response to excitation at the wellhead or at one end of a sealed interval, noting the possibility of matched resonance between tube waves in the wellbore and Krauklis waves in the fracture.

## Tube wave governing equations and wellbore-fracture coupling

Let $z$ be the distance along the well. The wellbore, with a constant radius $a$ and cross-sectional area $A_T = \pi a^2$, is intersected by a fracture at $z = 0$ with aperture $w_0$ at the fracture mouth. Low frequency tube waves are governed by the linearized momentum and mass balance equations (the latter combined with linearized constitutive laws for a compressible fluid and deformable elastic solid surrounding the wellbore):

$$\rho \frac{\partial v}{\partial t} + \frac{\partial p}{\partial z} = 0 \tag{21}$$

$$\frac{1}{M}\frac{\partial p}{\partial t} + \frac{\partial v}{\partial z} = -\alpha u(t)\delta(z), \tag{22}$$

where $v(z,t)$ is the cross-sectionally averaged particle velocity along the wellbore, $p(z,t)$ is pressure, $u(t)$ is the velocity into the fracture at the fracture mouth, $\rho$ is the fluid density (assumed to be the same as in the fracture), and $M$ is a modulus that is typically close to the fluid bulk modulus (Biot, 1952). Finally,

$$\alpha = A_f / A_T \tag{23}$$

is the ratio of the fracture mouth area $A_f$ to the wellbore cross-sectional area $A_T$. For a fracture intersecting the wellbore perpendicularly, as we assume in the examples presented below, $A_f = 2\pi a w_0$ and hence $\alpha = 2w_0/a$. This can be generalized to account for fractures intersecting the wellbore at other angles (Hornby et al., 1989; Derov et al., 2009). These equations describe nondispersive wave propagation at tube wave speed $c_T = \sqrt{M/\rho}$. In all examples shown below, we set the wellbore diameter to $2a = 0.1$ m and assume $M = K$ (and hence $c_T = c_0$) for simplicity, though expressions are given for the general case. The model can, of course, be generalized to account for permeable walls (Tang, 1990), irregularly shaped boreholes (Tezuka et al., 1997), spatially variable properties (Chen et al., 1996; Wang et al., 2008), and friction (Livescu et al., 2016). The source term on the right-hand side of the mass balance equation 22 describes the mass exchange between the wellbore and the fracture at the fracture mouth. Since the fracture aperture is much smaller than the tube wave wavelength, the source term is approximately a delta function at the fracture location.

Integrating equations 21 and 22 across the junction at the wellbore-fracture intersection, we obtain the following jump conditions:

$$v(0^+, t) - v(0^-, t) = -\alpha u(t), \tag{24}$$

$$p(0^+, t) - p(0^-, t) = 0. \tag{25}$$

The pressure is continuous across the junction, whereas the velocity through the wellbore experiences a jump that accounts for mass exchange with the fracture. The fluid velocity into the fracture, $u(t)$, is related to the pressure at the fracture mouth, $p(0, t)$, through the fracture transfer function using equation 15. By Fourier transforming equations 24 and 25 and using equation 15, we obtain

$$\hat{v}(0^+, \omega) - \hat{v}(0^-, \omega) = -\frac{\alpha F(\omega)}{\rho c_0}\hat{p}(0, \omega). \tag{26}$$

## Tube wave reflection/transmission coefficients

We now derive the reflection and transmission coefficients of tube waves incident on the fracture. Assuming an infinitely long well, we seek a Fourier-domain solution of the form

$$\hat{p}(z,\omega) = \begin{cases} e^{ikz} + Re^{-ikz}, & z < 0, \\ Te^{ikz}, & z > 0, \end{cases} \tag{27}$$

where $k = \omega/c_T$ is the wavenumber, the incident wave has unit amplitude, and $R$ and $T$ are the reflection and transmission coefficients. Satisfying the governing equations 21 and 22 and the fracture junction conditions (equations 25 and 26) yields

$$R(\omega) = -\frac{r(\omega)/2}{1 + r(\omega)/2} = -\frac{1}{1 + 2/r(\omega)}, \tag{28}$$

$$T(\omega) = \frac{1}{1 + r(\omega)/2} = \frac{2/r(\omega)}{1 + 2/r(\omega)}, \tag{29}$$

in which

$$r(\omega) = \frac{\alpha F(\omega) c_T}{c_0} = \frac{Z_f(\omega)/A_f}{\rho c_T/A_T} \tag{30}$$

is the ratio of the fracture hydraulic impedance, $Z_f(\omega)/A_f$, to the hydraulic impedance of tube waves in the wellbore, $\rho c_T/A_T$. Hydraulic impedance is defined as the ratio of volumetric flow (velocity times cross-sectional area) to pressure. The factor of two in the expressions for $R(\omega)$ and $T(\omega)$ arises because a pair of tube waves propagate away from the fracture.

Figure 9 explores the relation between the fracture transfer function and the reflection/transmission coefficients. Maximum reflection approximately coincides with the resonance peaks in the transfer functions, corresponding to the eigenmodes of the fracture with constant pressure boundary condition at the fracture mouth. At these frequencies the hydraulic impedance of the fracture greatly exceeds that of tube waves (i.e., $r(\omega)/2 \gg 1$),

and only small pressure changes at the fracture mouth are required to induce large flow into or out of the fracture. The reflection coefficient goes to $-1$ in this limit, so that waves at these specific frequencies are reflected as if from a constant pressure boundary. We also note that reducing the fracture width decreases reflection, both because the fracture mouth area decreases relative to the wellbore cross-sectional area (captured in $\alpha$) and because the fracture resonance peak amplitude decreases due to increased viscous dissipation in narrower fractures (captured in $F$).

## Response of wellbore-fracture system

We now consider a finite-length section of the well intersected by a single fracture, with boundary conditions prescribed at both ends of the well section. These ends might coincide with the wellhead and well bottom or the two ends of a sealed interval. Let $h_1$ and $h_2$ be the lengths of the two sections above and below the fracture, respectively, with the fracture at $z = 0$ as before. We seek the pressure and velocity within the wellbore, given excitation at the end of the upper well section.

Equations 21 and 22 are supplemented with boundary conditions at the top and bottom of the wellbore. At the top ($z = -h_1$), we prescribe velocity:

$$v(-h_1, t) = V(t) = Q(t)/A_T, \tag{31}$$

where $V(t)$ is the imposed velocity and $Q(t)$ is the associated volumetric injection rate. In Appendix B we show that this boundary condition is mathematically equivalent to the case of a sealed end (that is, $v(-h_1, t) = 0$) with a monopole source placed within the wellbore just below the end. At the bottom ($z = h_2$) we assume a partially reflecting condition of

the form

$$p(h_2,t) - \rho c_T v(h_2,t) = R_b \left[p(h_2,t) - \rho c_T v(h_2,t)\right], \tag{32}$$

in which $R_b$ is the well bottom reflection coefficient (satisfying $|R_b| \leq 1$). This boundary condition can equivalently be written in terms of the impedance $Z_b$ at the bottom of the well:

$$p(h_2,t) = Z_b v(h_2,t), \quad Z_b = \frac{1+R_b}{1-R_b}\rho c_T. \tag{33}$$

We assume constant, real $R_b$ (and hence $Z_b$), though it is possible to use a frequency-dependent, complex-valued $R_b$ if desired. For $R_b = 0$ there is no reflection from the bottom, $R_b = 1$ corresponds to $v(h_2,t) = 0$, and $R_b = -1$ corresponds to $p(h_2,t) = 0$.

The solution to the stated problem is

$$\hat{p}(z,\omega) = \begin{cases} a_1 \sin(kz) + a_2 \cos(kz), & -h_1 < z < 0, \\ b_1 e^{ikz} + b_2 e^{-ikz}, & 0 < z < h_2, \end{cases} \tag{34}$$

$$\rho c_T \hat{v}(z,\omega) = \begin{cases} -ia_1 \cos(kz) + ia_2 \sin(kz), & -h_1 < z < 0, \\ b_1 e^{ikz} - b_2 e^{-ikz}, & 0 < z < h_2, \end{cases} \tag{35}$$

where $k = \omega/c_T$ and the coefficients $a_1$, $a_2$, $b_1$, and $b_2$ are determined by the top boundary condition (equation 31), bottom boundary condition (equation 32), and fracture junction conditions (equations 25 and 26):

$$a_1 = \frac{i\rho c_T \hat{V}(\omega)}{D(\omega)}, \tag{36}$$

$$a_2 = \frac{\rho c_T \hat{V}(\omega)}{\left[r(\omega) + \Lambda(\omega)\right] D(\omega)}, \tag{37}$$

$$b_1 = \frac{\rho c_T \hat{V}(\omega)}{\left(1 + R_b e^{2ikh_2}\right)\left[r(\omega) + \Lambda(\omega)\right] D(\omega)}, \tag{38}$$

$$b_2 = \frac{R_b e^{2ikh_2} \rho c_T \hat{V}(\omega)}{\left(1 + R_b e^{2ikh_2}\right)\left[r(\omega) + \Lambda(\omega)\right] D(\omega)}, \tag{39}$$

where

$$D(\omega) = \cos(kh_1) - \frac{i\sin(kh_1)}{r(\omega) + \Lambda(\omega)}, \tag{40}$$

$$\Lambda(\omega) = \frac{1 - R_b e^{2ikh_2}}{1 + R_b e^{2ikh_2}}, \tag{41}$$

and $r(\omega)$ is the hydraulic impedance ratio defined as before (equation 30). Solutions in the time domain are obtained by inverting the Fourier transform.

## Excitation at the wellhead

Here we utilize the solution derived above to demonstrate how fracture growth might be monitored using tube waves or water hammer signals generated by excitation at the wellhead. The wellbore has a total length of 3 km, a diameter of $2a = 0.1$ m, and a partially sealed bottom with reflection coefficient $R_b = 0.8$. A single fracture is placed 2 km from the wellhead and 1 km from the well bottom (i.e., $h_1 = 2$ km and $h_2 = 1$ km). At the wellhead, we prescribe a broadband chirp (up to ~500 Hz) in velocity, as shown in Figure 10. As mentioned earlier and detailed in Appendix B, this is equivalent to placing a monopole source a short distance below the sealed wellhead. To account for dissipation during tube wave propagation along the wellbore, we add a small imaginary part to the tube wave speed: $c_T = (1 - 10^{-3}i)\sqrt{M/\rho}$. Figure 11 shows a schematic of this system and the synthetic borehole record section. The interplay between tube waves in the wellbore and dispersive Krauklis waves within the fracture is evident.

## Matched resonance

The example shown in Figure 11 illustrates the response when the entire, long wellbore is hydraulically connected to the fracture. Distinct reflections can be seen and interference

between different reflections is confined to short time intervals. We next examine the more complex response that arises when a much smaller section of the well around the fracture is sealed at both ends, and a source is placed at one end. The solution given in equations 34–41 still applies, but we select a smaller length $h_1$. There is now complex interference between multiply reflected waves; whether this interference is constructive or destructive depends on the well section lengths $h_1$ and $h_2$ and the fracture reflection/transmission coefficients (and hence frequency). As we demonstrate, the signals in the upper well section that contains the source can be selectively amplified when a resonance frequency of the upper well section is tuned to one of the resonance frequencies of the fracture. We refer to this phenomenon as matched resonance.

Reflection of waves from the fracture is most pronounced at frequencies that permit maximum exchange of fluid between the wellbore and fracture. These frequencies correspond approximately to the resonance frequencies of the fracture with a constant pressure boundary condition at the fracture mouth (i.e., corresponding to the peaks of the fracture transfer function; see Figure 9). The resonance frequencies of the upper wellbore section with a sealed top end ($v = 0$) and constant pressure condition ($p = 0$) at the fracture satisfy $\cos(\omega h_1/c_T) = 0$. For example, the lowest resonance frequency is $f = \omega/2\pi = c_T/4h_1$. Matched resonance occurs when one of these frequencies matches a fracture resonance frequency.

To justify this more rigorously, and explain some possible complications, note that the tube wave eigenfunctions associated with this resonant wellbore response are $\sin(\omega z/c_T)$, corresponding to the first term on the right-hand side of equation 34. The amplitude of this term is given by equation 36, which is largest when the denominator $D(\omega)$, given in equation 40, is smallest. The hydraulic impedance ratio is quite large (ideally, $|r(\omega)| \gg 1$)

around the fracture resonance frequencies. A further requirement is that $|\Lambda(\omega)|$ be sufficiently small compared to $|r(\omega)|$, at least around the targeted fracture resonance frequency. When these conditions are satisfied, $D(\omega) \approx \cos(kh_1)$ with $k = \omega/c_T$. Setting $D(\omega) = 0$ then yields the wellbore section resonance condition $\cos(\omega h_1/c_T) = 0$ stated above. Of course, this resonance condition is only an approximation, especially when $|r(\omega)|$ does not greatly exceed unity or when $|\Lambda(\omega)|$ is not small. In these cases, the matched resonance condition can be more precisely determined by finding the frequencies $\omega$ that minimize the exact $D(\omega)$ in equation 40. However, $\Lambda(\omega)$ can be made arbitrarily small by sealing the bottom end of the lower well section ($R_b = 1$ and hence $\Lambda(\omega) = -i\tan(\omega h_2/c_T)$) and decreasing $h_2$ such that $\omega h_2/c_T \ll 1$.

Figure 12a and b illustrates matched resonance. The frequency of the fundamental mode of the fracture (the 10-m-long, 5-mm-wide example shown in Figures 5 and 9) is $f \approx 3.8$ Hz, so the upper wellbore section is chosen to be $h_1 = 100$ m $\approx c_T/4f$ long to satisfy the matched resonance condition. The system is excited by a broadband chirp at the upper end of this wellbore section. The 3.8-Hz resonance frequency clearly dominates the system response. The response is shown for two bottom boundary conditions. The first is the relatively simple case of a well with a nonreflecting bottom boundary ($R_b = 0$, for which $\Lambda = 1$ regardless of $h_2$). This eliminates the possibility of resonance within the lower wellbore section, and prevents bottom reflections from then transmitting through the fracture to return to the upper well section. The second case has $h_2 = 10$ m and $R_b = 0.9$, corresponding to a partially sealed end a short distance below the fracture. While the initial response in the second case contains a complex set of high frequency reverberations associated with reflections within the lower well section, these are eventually damped out to leave only the prominent 3.8-Hz resonance. This illustrates a rather remarkable insensitivity

to characteristics of the lower well section, as similar results (not shown) were found even for a wide range of lower well section lengths $h_2$.

We next demonstrate how changing the length of the upper well section, $h_1$, alters the resonant response of the system. Figure 12c and d shows the response for values of $h_1$ that are both larger and smaller than the matched resonance length. The fundamental mode resonance peak shifts to a lower frequency when $h_1$ increases, and to a higher frequency when $h_1$ decreases. Many resonant modes are excited for the large $h_1$ case, leading to a rather complex pressure response. The situation is simpler for the small $h_1$ case, but as $h_1$ continues to decrease, the amplitude of the fundamental mode peak continues to decrease and might be difficult to observe in noisy data.

## CONCLUSIONS

We have investigated the interaction of tube waves with fractures. While this problem has received much attention in the literature, previous work has been restricted to relatively idealized analytical or semi-analytical models of the fracture response. In contrast, we advocate the use of numerical simulations to more accurately describe the fracture. These simulations account for variable fracture width, narrow viscous boundary layers adjacent to the fracture walls, and dissipation from both viscosity and seismic radiation. The simulations feature Krauklis waves propagating along the fracture; counterpropagating pairs of Krauklis waves form the eigenmodes of the fracture. As many authors have noted, the frequency and attenuation of these modes can be used to constrain fracture geometry.

While this initial study utilizes a two-dimensional plane strain fracture model, the overall methodology can be applied when three-dimensional models of the fracture are available.

Such models would permit investigation of fractures that have bounded height, a commonly arising situation in industry, and one for which the two-dimensional model presented here is not well justified.

We then showed how to distill the simulation results into a single, complex-valued function that quantifies the fracture response, specifically its hydraulic impedance (or the normalized reciprocal of the impedance, the fracture transfer function). The fracture transfer function can then be used to determine how tube waves within a wellbore reflect and transmit from fractures intersecting the well, and to solve for the response of the wellbore-fracture system to excitation at the wellhead or within the wellbore.

The coupled wellbore-fracture system has a particularly complex response, potentially involving resonance within wellbore sections adjacent to the fracture or within the fracture itself. We found that it is possible to selectively amplify tube waves at the eigenfrequencies of the fracture by properly choosing the length of the well section containing the source and intersecting the fracture. This phenomenon, which we term matched resonance, could prove useful to excite and measure fracture eigenmodes, which can then be used to infer the fracture geometry.



## ACKNOWLEDGMENTS

This work was supported by a gift from Baker Hughes to the Stanford Energy and Environment Affiliates Program and seed funding from the Stanford Natural Gas Initiative. O. O'Reilly was partially supported by the Chevron fellowship in the Department of Geophysics at Stanford University.

# APPENDIX A

## DISPERSION-BASED FRACTURE TRANSFER FUNCTION

In this appendix, we use the Krauklis wave dispersion relation to derive an approximate expression for the fracture transfer function. Let $x$ be the distance into the fracture measured from the fracture mouth at $x = 0$. The fracture has length $L$ and uniform aperture $w_0$. Solutions in the frequency domain are written as a superposition of plane waves propagating in the $+x$ and $-x$ directions:

$$\hat{p}(x,\omega) = Ae^{ikx} + Be^{-ikx}, \tag{A-1}$$

$$\rho c\hat{u}(x,\omega) = Ae^{ikx} - Be^{-ikx}, \tag{A-2}$$

where $k = k(\omega)$ and $c = \omega/k(\omega)$ are the wave number and phase velocity determined by the Krauklis wave dispersion relation (equation 8, solved for real $\omega$ and possibly complex $k$), and $A$ and $B$ are coefficients determined by boundary conditions at the ends of the fracture. At the fracture tip, the fluid velocity is set to zero:

$$\hat{u}(L,\omega) = Ae^{ikL} - Be^{-ikL} = 0. \tag{A-3}$$

The fracture transfer function, defined in equation 15, is obtained by combining equations A-1–A-3:

$$F(\omega) = \frac{-ik(\omega)c_0 \tan\left[k(\omega)L\right]}{\omega}. \tag{A-4}$$

Peaks in $F(\omega)$ correspond to the resonance frequencies of the fracture with a constant pressure condition at the fracture mouth. Therefore, besides equation A-3, we have

$$\hat{p}(0,\omega) = A + B = 0 \tag{A-5}$$

Combining equations A-3 and A-5, we obtain the resonance condition

$$\cos kL = 0, \tag{A-6}$$

or $k_n = (n - 1/2)\pi$ for positive integers $n = 1, 2, \ldots$. This can be solved, assuming real $k$ and complex $\omega$, for the resonance frequencies and (temporal) decay rates of the eigenmodes.

We next derive the resonance frequencies for the case of negligible dissipation (i.e., for an inviscid fluid). In this case, both $k$ and $\omega$ are real and we have (Krauklis, 1962)

$$c(\omega) = (G^* w_0 \omega / 2\rho)^{1/3} = (G^* w_0 \pi f / \rho)^{1/3}. \tag{A-7}$$

It follows that the resonance frequencies are

$$f_n = \sqrt{(\pi G^* w_0 / \rho)[(n - 1/2)/2L]^3}. \tag{A-8}$$

This expression provides a reasonably accurate prediction of the resonance frequencies for the examples shown in this work, provided that $w_0$ in equation A-8 is interpreted as average width.

## APPENDIX B

## EQUIVALENCE OF MONOPOLE SOURCE AND VELOCITY BOUNDARY CONDITION

In this appendix, we establish the equivalence, for sufficiently low frequencies, between a monopole source placed just below the sealed end of a wellbore section and a prescribed velocity boundary condition at that end. For convenience we take $z = 0$ to coincide with the end. The tube wave equations with a monopole source $m(t)$ at $z = s$ are

$$\frac{1}{M}\frac{\partial p}{\partial t} + \frac{\partial v}{\partial z} = m(t)\delta(z - s), \tag{B-1}$$

$$\rho\frac{\partial v}{\partial t} + \frac{\partial p}{\partial z} = 0. \tag{B-2}$$

For the sealed end, $v(0,t) = 0$, whereas the prescribed velocity boundary condition is

$$v(0,t) = V(t). \tag{B-3}$$

We now show equivalence of these two problems, in the sense that $V(t) \approx m(t)$, for frequencies satisfying

$$s\omega/c_T \ll 1. \tag{B-4}$$

This is done by requiring that the outgoing waves below the source ($z > s$) are identical for the two problems.

The solution to equations B-1 and B-2 in a semi-infinite wellbore with zero velocity at $z = 0$ is

$$\hat{p}(z,\omega) = \begin{cases} a\cos(\omega z/c_T), & 0 < z < s, \\ be^{i\omega(z-s)/c_T}, & z > s, \end{cases} \tag{B-5}$$

$$\rho c_T \hat{v}(z,\omega) = \begin{cases} ia\sin(\omega z/c_T), & 0 < z < s, \\ be^{i\omega(z-s)/c_T}, & z > s, \end{cases} \tag{B-6}$$

where $a$ and $b$ are constants to be determined.

Fourier transforming equations B-1 and B-2 and integrating across the source yields the jump conditions across the source:

$$\hat{p}(s^+,\omega) - \hat{p}(s^-,\omega) = 0, \tag{B-7}$$

$$\hat{v}(s^+,\omega) - \hat{v}(s^-,\omega) = \hat{m}(\omega). \tag{B-8}$$

Constants $a$ and $b$ are determined by substituting equations B-5 and B-6 into equations

B-7 and B-8:

$$a = \rho c_T \hat{m}(\omega) e^{is\omega/c_T}, \tag{B-9}$$

$$b = \rho c_T \hat{m}(\omega) \cos(s\omega/c_T) e^{is\omega/c_T}. \tag{B-10}$$

Substituting equations B-9 and B-10 into equations B-5 and B-6, we obtain the solution below the source ($z > s$):

$$\hat{p}(z,\omega) = \rho c_T \hat{m}(\omega) \cos(s\omega/c_T) e^{i\omega z/c_T}, \tag{B-11}$$

$$\hat{v}(z,\omega) = \hat{m}(\omega) \cos(s\omega/c_T) e^{i\omega z/c_T}, \tag{B-12}$$

Similarly, we obtain the solution to the tube wave problem with no internal source but with the top boundary condition being $v(0,t) = V(t)$:

$$\hat{p}(z,\omega) = \rho c_T \hat{V}(\omega) e^{i\omega z/c}, \tag{B-13}$$

$$\hat{v}(z,\omega) = \hat{V}(\omega) e^{i\omega z/c}. \tag{B-14}$$

We now determine the condition for which the wave field below the source ($z > s$) is identical between the two problems. Specifically, we require equivalence of equations B-11 and B-13 and similarly for equations B-12 and B-14. The necessary condition is

$$\hat{V}(\omega) = \hat{m}(\omega) \cos(s\omega/c_T). \tag{B-15}$$

Moreover, for sources placed just below the sealed end, or equivalently at sufficiently low frequencies, $s\omega/c_T \ll 1$ and $\cos(s\omega/c_T) \approx 1$. Thus, $\hat{V}(\omega) \approx \hat{m}(\omega)$ or $V(t) \approx m(t)$ as claimed.

## REFERENCES

Aki, K., M. Fehler, and S. Das, 1977, Source mechanism of volcanic tremor: Fluid-driven crack models and their application to the 1963 kilauea eruption: Journal of Volcanology and Geothermal Research, **2**, 259–287.

Bakku, S. K., M. Fehler, and D. Burns, 2013, Fracture compliance estimation using borehole tube waves: Geophysics, **78**, D249–D260.

Batchelor, G. K., 2000, An introduction to fluid dynamics: Cambridge University Press.

Beydoun, W. B., C. H. Cheng, and M. N. Toksz, 1985, Detection of open fractures with vertical seismic profiling: Journal of Geophysical Research: Solid Earth, **90**, 4557–4566.

Biot, M., 1952, Propagation of elastic waves in a cylindrical bore containing a fluid: Journal of Applied Physics, **23**, 997–1005.

Candela, T., F. Renard, Y. Klinger, K. Mair, J. Schmittbuhl, and E. E. Brodsky, 2012, Roughness of fault surfaces over nine decades of length scales: Journal of Geophysical Research: Solid Earth, **117**, n/a–n/a. (B08409).

Carey, M. A., S. Mondal, and M. M. Sharma, 2015, Analysis of water hammer signatures for fracture diagnostics: Presented at the SPE Annual Technical Conference and Exhibition, Society of Petroleum Engineers.

Chen, X., Y. Quan, and J. M. Harris, 1996, Seismogram synthesis for radially layered media using the generalized reflection/transmission coefficients method: Theory and applications to acoustic logging: Geophysics, **61**, 1150–1159.

Chen, Y., and L. Knopoff, 1986, Static shear crack with a zone of slip-weakening: Geophysical Journal International, **87**, 1005–1024.

Chouet, B., 1986, Dynamics of a fluid-driven crack in three dimensions by the finite difference method: Journal of Geophysical Research: Solid Earth, **91**, 13967–13992.

———, 1988, Resonance of a fluid-driven crack: Radiation properties and implications for the source of long-period events and harmonic tremor: Journal of Geophysical Research: Solid Earth, **93**, 4375–4400.

Derov, A., G. Maximov, M. Lazarkov, B. Kashtan, and A. Bakulin, 2009, Characterizing hydraulic fractures using slow waves in the fracture and tube waves in the borehole: Presented at the 2009 SEG Annual Meeting, Society of Exploration Geophysicists.

Dunham, E. M., D. Belanger, L. Cong, and J. E. Kozdon, 2011, Earthquake ruptures with strongly rate-weakening friction and off-fault plasticity, part 2: Nonplanar faults: Bulletin of the Seismological Society of America, **101**, 2308–2322.

Dunham, E. M., and D. E. Ogden, 2012, Guided waves along fluid-filled cracks in elastic solids and instability at high flow rates: Journal of Applied Mechanics, **79**, 031020.

Ferrazzini, V., and K. Aki, 1987, Slow waves trapped in a fluid-filled infinite crack: Implication for volcanic tremor: Journal of Geophysical Research: Solid Earth, **92**, 9215–9223.

Frehner, M., 2013, Krauklis wave initiation in fluid-filled fractures by seismic body waves: Geophysics, **79**, T27–T35.

Frehner, M., and S. M. Schmalholz, 2010, Finite-element simulations of stoneley guided-wave reflection and scattering at the tips of fluid-filled fractures: Geophysics, **75**, T23–T36.

Henry, F., 2005, Characterization of borehole fractures by the body and interface waves: TU Delft, Delft University of Technology.

Henry, F., J. Fokkema, and C. de Pater, 2002, Experiments on stoneley wave propagation in a borehole intersected by a finite horizontal fracture: Presented at the 64th EAGE Conference & Exhibition.

Holzhausen, G., and H. Egan, 1986, Fracture diagnostics in east texas and western col-

orado using the hydraulic-impedance method: Presented at the SPE Unconventional Gas Technology Symposium, Society of Petroleum Engineers.

Holzhausen, G., and R. Gooch, 1985a, Impedance of hydraulic fractures: its measurement and use for estimating fracture closure pressure and dimensions: Presented at the SPE/DOE Low Permeability Gas Reservoirs Symposium, Society of Petroleum Engineers.

Holzhausen, G. R., and R. P. Gooch, 1985b, The effect of hydraulic-fracture growth on free oscillations of wellbore pressure: Presented at the The 26th US Symposium on Rock Mechanics (USRMS), American Rock Mechanics Association.

Hornby, B., D. Johnson, K. Winkler, and R. Plumb, 1989, Fracture evaluation using reflected stoneley-wave arrivals: Geophysics, **54**, 1274–1288.

Ionov, A. M., 2007, Stoneley wave generation by an incident p-wave propagating in the surrounding formation across a horizontal fluid-filled fracture: Geophysical Prospecting, **55**, 71–82.

Ionov, A. M., and G. A. Maximov, 1996, Propagation of tube waves generated by an external source in layered permeable rocks: Geophysical Journal International, **124**, 888–906.

Korneev, V., 2008, Slow waves in fractures filled with viscous fluid: Geophysics, **73**, N1–N7.

———, 2010, Low-frequency fluid waves in fractures and pipes: Geophysics, **75**, N97–N107.

Kostek, S., D. L. Johnson, and C. J. Randall, 1998a, The interaction of tube waves with borehole fractures, part i: Numerical models: Geophysics, **63**, 800–808.

Kostek, S., D. L. Johnson, K. W. Winkler, and B. E. Hornby, 1998b, The interaction of tube waves with borehole fractures, part ii: Analytical models: Geophysics, **63**, 809–815.

Krauklis, P. V., 1962, On some low-frequency oscillations of a fluid layer in an elastic medium: Prikl. Mat. Mekh., **26**, 1111–1115.

Krauklis, P. V., and L. Krauklis, 1998, Excitation of a tube wave in a borehole by a slow

wave propagating in a fluid layer: J. Math. Sci., **91**, 2776–2781.

Lawn, B., 1993, Fracture of brittle solids: Cambridge University Press.

Lipovsky, B. P., and E. M. Dunham, 2015, Vibrational modes of hydraulic fractures: Inference of fracture geometry from resonant frequencies and attenuation: Journal of Geophysical Research: Solid Earth, **120**, 1080–1107.

Livescu, S., S. Craig, and B. Aitken, 2016, Fluid-hammer effects on coiled-tubing friction in extended-reach wells: SPE Journal, SPE–179100–PA.

Mathieu, F., and M. Toksoz, 1984, Application of full waveform acoustic logging data to the estimation of reservoir permeability: Technical report, Massachusetts Institute of Technology. Earth Resources Laboratory.

Medlin, W., and D. Schmitt, 1994, Fracture diagnostics with tube wave reflection logs: Journal of Petroleum Technology, **46**, 239–248.

Mondal, S., 2010, Pressure transients in wellbores: water hammer effects and implications for fracture diagnostics: Master's thesis, The University of Texas at Austin.

Nakagawa, S., 2013, Low-frequency (<100 hz) dynamic fracture compliance measurement in the laboratory: Presented at the 47th US Rock Mechanics/Geomechanics Symposium, American Rock Mechanics Association.

Nakagawa, S., S. Nakashima, and V. A. Korneev, 2016, Laboratory measurements of guided-wave propagation within a fluid-saturated fracture: Geophysical Prospecting, **64**, 143–156.

Nikitin, A. A., B. D. Plyushchenkov, and A. Y. Segal, 2016, Properties of low-frequency trapped mode in viscous-fluid waveguides: Geophysical Prospecting, **64**, 1335–1349.

OReilly, O., E. Dunham, and D. Moos, 2014, Inferring the properties of fluid-filled fractures using tube waves: AGU Fall Meeting Abstracts, 4799.

Paige, R., L. Murray, and J. Roberts, 1995, Field application of hydraulic impedance testing for fracture measurement: SPE production & Facilities, **10**, 7–12.

Paige, R., J. Roberts, L. Murray, and D. Mellor, 1992, Fracture measurement using hydraulic impedance testing: Presented at the SPE Annual Technical Conference and Exhibition, Society of Petroleum Engineers.

Paillet, F., and J. White, 1982, Acoustic modes of propagation in the borehole and their relationship to rock properties: Geophysics, **47**, 1215–1228.

Paillet, F. L., 1980, Acoustic propagation in the vicinity of fractures which intersect a fluid-filled borehole: Presented at the SPWLA 21st Annual Logging Symposium, Society of Petrophysicists and Well-Log Analysts. (SPWLA-1980-DD).

Patzek, T. W., and A. De, 2000, Lossy transmission line model of hydrofractured well dynamics: Journal of Petroleum Science and Engineering, **25**, 59–77.

Power, W. L., and T. E. Tullis, 1991, Euclidean and fractal models for the description of rock surface roughness: Journal of Geophysical Research: Solid Earth, **96**, 415–424.

Schoenberg, M., 1986, Fluid and solid motion in the neighborhood of a fluid-filled borehole due to the passage of a low-frequency elastic plane wave: Geophysics, **51**, 1191–1205.

Shih, P.-J. R., and M. Frehner, 2015, Laboratory evidence for krauklis wave resonance in a fracture and implications for seismic coda wave analysis: Presented at the 2015 SEG Annual Meeting, Society of Exploration Geophysicists.

Tang, X., 1990, Acoustic logging in fractured and porous formations: PhD thesis, Massachusetts Institute of Technology.

Tang, X. M., and C. H. Cheng, 1988, Wave propagation in a fluid-filled fracture an experimental study: Geophysical Research Letters, **15**, 1463–1466.

———, 1989, A dynamic model for fluid flow in open borehole fractures: Journal of Geo-

physical Research: Solid Earth, **94**, 7567–7576.

Tary, J. B., M. van der Baan, and D. W. Eaton, 2014, Interpretation of resonance frequencies recorded during hydraulic fracturing treatments: Journal of Geophysical Research: Solid Earth, **119**, 1295–1315.

Tezuka, K., C. H. Cheng, and X. M. Tang, 1997, Modeling of low-frequency stoneley-wave propagation in an irregular borehole: Geophysics, **62**, 1047–1058.

Wang, X., K. Hovem, D. Moos, and Y. Quan, 2008, Water hammer effects on water injection well performance and longevity: Presented at the SPE International Symposium and Exhibition on Formation Damage Control, Society of Petroleum Engineers. (SPE 112282-PP).

Yamamoto, M., and H. Kawakatsu, 2008, An efficient method to compute the dynamic response of a fluid-filled crack: Geophysical Journal International, **174**, 1174–1186.

Ziatdinov, S., B. Kashtan, and A. Bakulin, 2006, Tube waves from a horizontal fluid-filled fracture of a finite radius: Presented at the 2006 SEG Annual Meeting, Society of Exploration Geophysicists.

# LIST OF TABLES

# LIST OF FIGURES

1 Tube waves, excited at the wellhead, are incident on a fluid-filled fracture intersecting the wellbore. Pressure changes and fluid mass exchange between the wellbore and fracture excite Krauklis waves within the fracture, leading to partial reflection of tube waves and dissipation of energy.

2 Snapshots from simulation of Krauklis waves and elastic waves excited by an imposed pressure chirp at the fracture mouth, for a 10-m-long fracture with 4-mm width at the fracture mouth. Background shows solid response (to scale) and inset shows fluid response (vertically exaggerated). Colors in solid show particle velocity in direction normal to the fracture walls; discontinuities across the fracture indicate opening/closing motions characteristic of Krauklis waves. Colors in fluid show particle velocity; note narrow viscous boundary layers near nonplanar fracture walls.

3 (a) Phase velocity and (b) spatial attenuation of Krauklis waves for real frequency. (c) Phase velocity and (d) temporal attenuation for real wavelength. Dispersion and attenuation curves are plotted for four fracture widths: 0.5 mm, 1 mm, 3 mm, and 10 mm, as labeled. Black and red dashed lines in (a) and (b) mark characteristic frequencies $f_{vis}$ and $f_{el}$ defined in text. Dashed lines in (c) and (d) mark the cutoff wavelength $\lambda_c$, beyond which waves cease to propagate.

4 Response of fractures to (a) broadband pressure chirp at the fracture mouth, quantified through (b) width-averaged velocity at the fracture mouth. The response, shown for five fractures having the same length ($L = 10$ m) and different widths (value given above each curve), is characterized by several resonance frequencies. The resonance frequency decreases as width decreases, as anticipated from the dependence of Krauklis wave phase velocity on width (equation 11 and Figure 3a). Higher frequencies decay quickly, leaving

only the fundamental resonant mode. Wider fractures experience less viscous dissipation (Figure 3b) and hence oscillate longer.

5 Fracture transfer function, $F(\omega)$, for a 10-m-long fracture with 5-mm width at the fracture mouth and profile shown in Figure 6a. (a) Real and imaginary parts of $F(\omega)$. Inset shows low frequency response, which is compared to the quasi-static approximation (equation 19) utilized in hydraulic impedance testing. Also shown are (b) amplitude and (c) phase of $F(\omega)$.

6 Fracture transfer functions for different fracture lengths and widths. (a) Normalized fracture geometry with fracture tip width equal to 1/50 of the width at the fracture mouth. (b) Fracture transfer functions for 4.7-mm-wide fractures with varied lengths. Longer fractures have lower resonance frequencies. (c) Fracture transfer functions for 3.6-m-long fractures with varied widths. Wider fractures have higher resonance frequencies. In panels (b) and (c), dashed lines plot the quasi-static limit (equation 19).

7 (a) Geometry of a 1 m long fracture with the tip width varied from 1, 1/5, 1/20, to 1/50 of the width at the fracture mouth (2 mm). (b) Amplitude of fracture transfer function with varied fracture tip width compared to the dispersion-based approximation solution (equation 20) and the quasi-static limit (equation 19).

8 (a) Graphical method to determine fracture length and width from frequency (red curves) and temporal quality factor $Q$ (black curves) of the fundamental resonant mode (i.e., from the fracture transfer function from numerical simulations employing the tapered fracture geometry; see Figure 6). In the overdamped region ($Q < 0.5$) viscous dissipation prevents resonant oscillations and geometry cannot be determined with this method. (b) Quality factor and (c) frequency, comparing numerical simulation results with solutions based on the dispersion relation (equation 8).

9 (a) Amplitude of fracture transfer functions, $|F|$, for two 10-m-long fractures with different widths (1 mm and 5 mm). (b) Amplitude of tube wave reflection and transmission coefficients, $|R|$ and $|T|$, across the fracture (equations 28 and 29) for wellbore diameter $2a = 0.1$ m. Maximum reflection occurs at the resonance frequencies of the fracture.

10 Chirp used for examples shown in Figures 11 and 12: (a) time series and (b) spectrum.

11 Response of the wellbore-fracture system to chirp excitation (Figure 10) at the wellhead. (a) Schematic of the system, with one fracture 2 km below the wellhead and 1 km above the well bottom. Sensor TP is 500 m above the fracture and sensor BT is 250 m below the fracture. (b) Record section of pressure along the wellbore (every 250 m) with a fracture that is 10 m long and 2 mm wide at the fracture mouth. Multiple reflections from the fracture, well bottom, and wellhead are observed. Dashed boxes mark the time window (1.5 s to 2.2 s) examined in (c) and (d) for sensors TP and BT. (c) Comparison of pressure at sensors TP and BT for fractures with same width but different lengths. (d) Same as (c) but for fractures with the same length but different widths. In (c) and (d), sensor TP shows waves reflected from the fracture; first arriving are direct tube wave reflections from the fracture mouth, followed by tube waves generated by Krauklis waves in the fracture that have reflected from the fracture tip. Sensor BT shows transmitted waves, which have similar arrivals. Longer fractures show a more dispersed set of Krauklis wave arrivals. Reflections are smaller from narrower fractures.

12 Matched resonance: the length of the upper wellbore section containing the source is chosen so that the resonance frequency of tube waves in this wellbore section matches the fundamental mode resonance frequency of the fracture (3.8 Hz). (a) Pressure response at a receiver in the center of the upper wellbore section (at $z = -h_1/2$) to the chirp excitation

shown in Figure 10. The 3.8-Hz resonance is selectively amplified, regardless of the length of the lower wellbore section and the bottom boundary condition: compare case with non-reflecting well bottom (red, $R_b = 0$) to partially sealed (blue, $R_b = 0.9$ and $h_2 = 10$ m). (b) Fourier amplitude spectrum of pressure time series shown in (a), with prominent peak at the 3.8-Hz matched resonance frequency. While additional spectral peaks appear for the sealed bottom case, the matched resonance peak is nearly identical to the nonreflecting bottom case. Also shown is the reflection coefficient of tube waves from the fracture, which has peaks at the fracture resonance frequencies. (c) Same as (a) but for $h_1 = 200$ m and 50 m (both with $R_b = 0.9$ and $h_2 = 10$ m). The system does not satisfy the matched resonance condition and the spectrum, shown in (d), is more complicated and lacks the pronounced peak at the fundamental resonance mode.

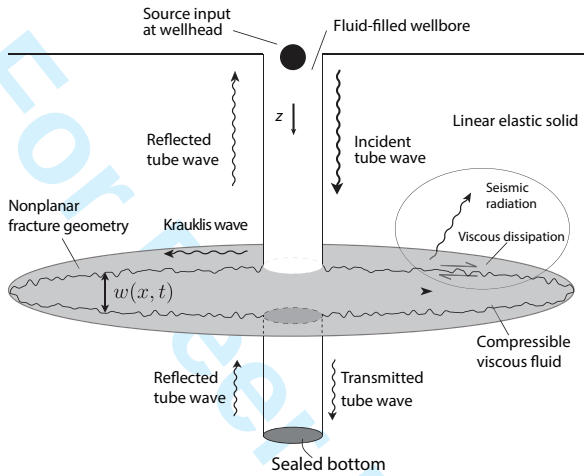


Figure 1: Tube waves, excited at the wellhead, are incident on a fluid-filled fracture intersecting the wellbore. Pressure changes and fluid mass exchange between the wellbore and fracture excite Krauklis waves within the fracture, leading to partial reflection of tube waves and dissipation of energy.

–

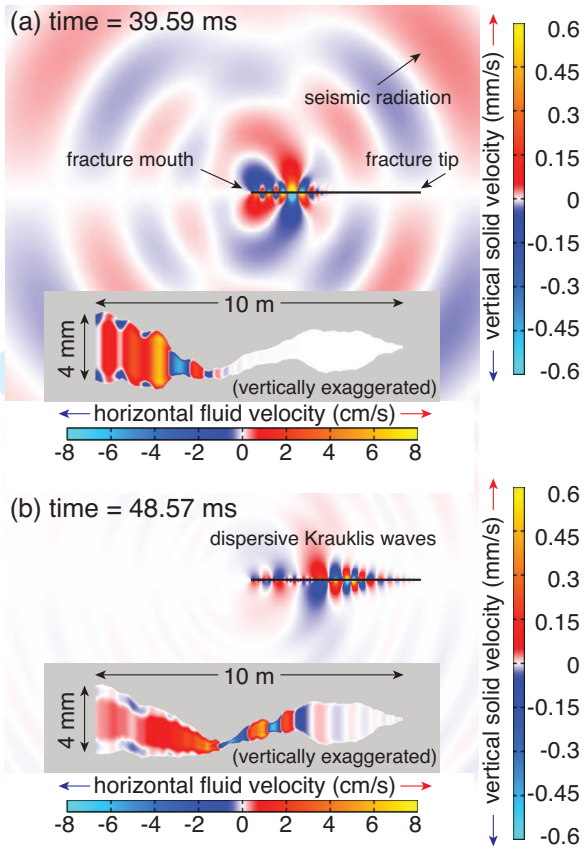


Figure 2: Snapshots from simulation of Krauklis waves and elastic waves excited by an imposed pressure chirp at the fracture mouth, for a 10-m-long fracture with 4-mm width at the fracture mouth. Background shows solid response (to scale) and inset shows fluid response (vertically exaggerated). Colors in solid show particle velocity in direction normal to the fracture walls; discontinuities across the fracture indicate opening/closing motions characteristic of Krauklis waves. Colors in fluid show particle velocity; note narrow viscous boundary layers near nonplanar fracture walls.

| | |
|---|---|
| Solid (rock) | |
| Density $\rho_s$ (kg/m$^3$) | 2489 |
| P Wave Speed, $c_p$ (m/s) | 4367 |
| S Wave Speed, $c_s$ (m/s) | 2646 |
| Fluid (water) | |
| Density $\rho_0$ (kg/m$^3$) | 1000 |
| Sound Wave Speed, $c_0$ (m/s) | 1500 |
| Viscosity, $\mu$ (Pa.s) | 0.001 |

Table 1: Material properties.

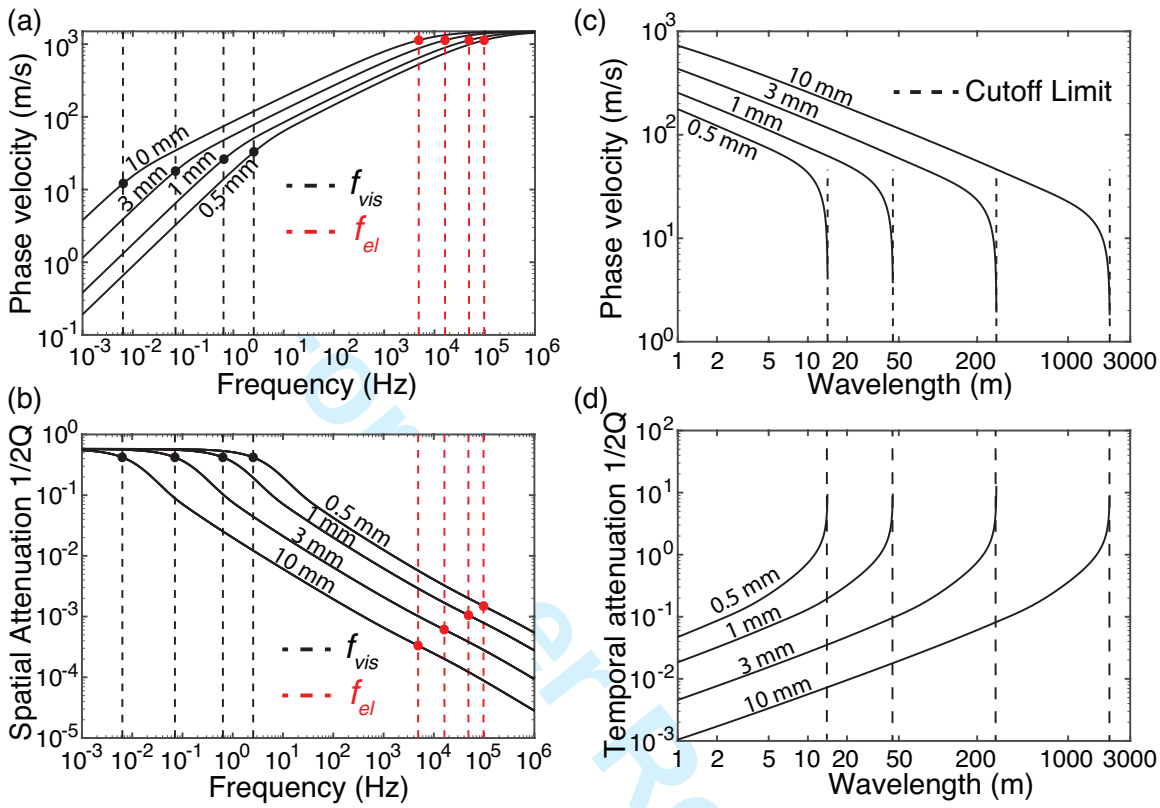


Figure 3: (a) Phase velocity and (b) spatial attenuation of Krauklis waves for real frequency. (c) Phase velocity and (d) temporal attenuation for real wavelength. Dispersion and attenuation curves are plotted for four fracture widths: 0.5 mm, 1 mm, 3 mm, and 10 mm, as labeled. Black and red dashed lines in (a) and (b) mark characteristic frequencies $f_{vis}$ and $f_{el}$ defined in text. Dashed lines in (c) and (d) mark the cutoff wavelength $\lambda_c$, beyond which waves cease to propagate.

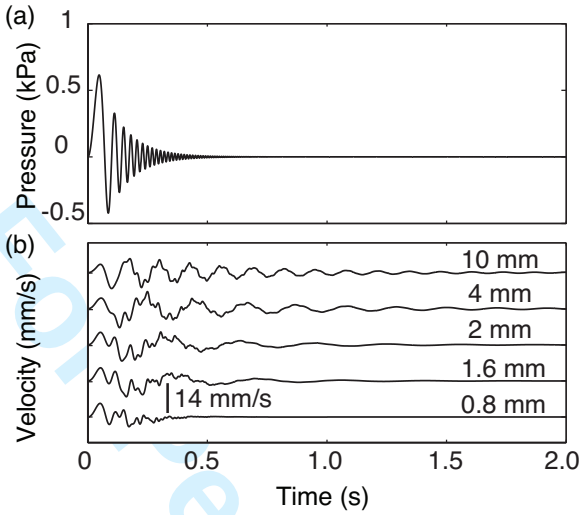


Figure 4: Response of fractures to (a) broadband pressure chirp at the fracture mouth, quantified through (b) width-averaged velocity at the fracture mouth. The response, shown for five fractures having the same length ($L = 10$ m) and different widths (value given above each curve), is characterized by several resonance frequencies. The resonance frequency decreases as width decreases, as anticipated from the dependence of Krauklis wave phase velocity on width (equation 11 and Figure 3a). Higher frequencies decay quickly, leaving only the fundamental resonant mode. Wider fractures experience less viscous dissipation (Figure 3b) and hence oscillate longer.

–

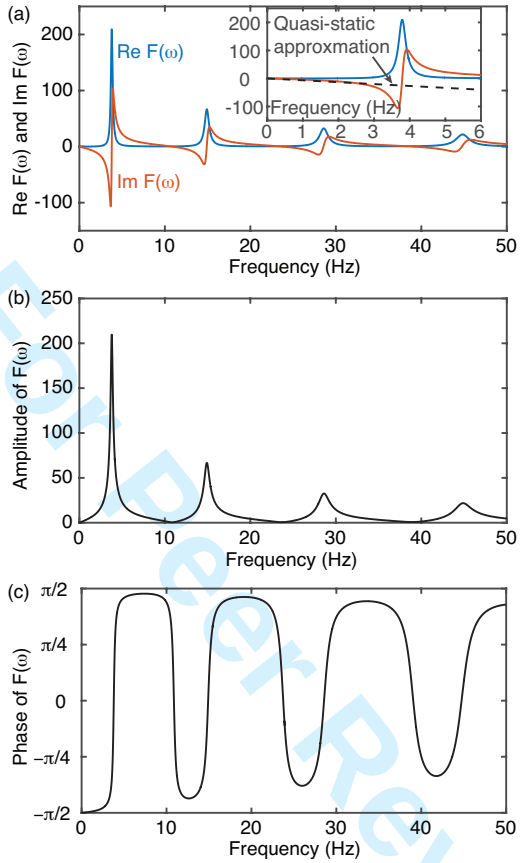


Figure 5: Fracture transfer function, $F(\omega)$, for a 10-m-long fracture with 5-mm width at the fracture mouth and profile shown in Figure 6a. (a) Real and imaginary parts of $F(\omega)$. Inset shows low frequency response, which is compared to the quasi-static approximation (equation 19) utilized in hydraulic impedance testing. Also shown are (b) amplitude and (c) phase of $F(\omega)$.

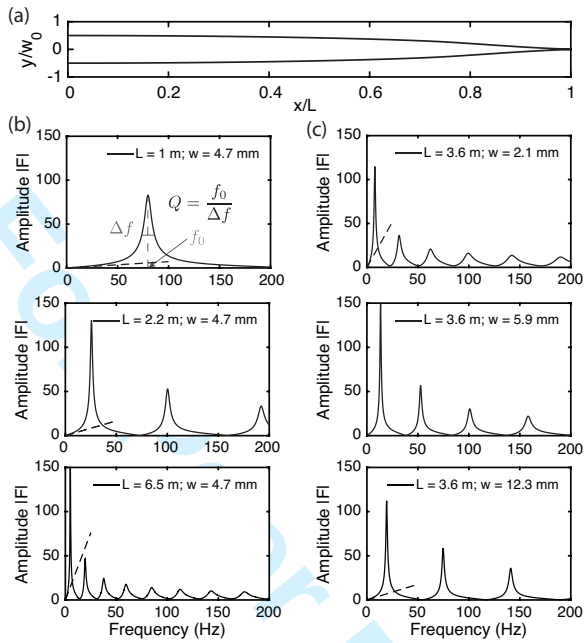


Figure 6: Fracture transfer functions for different fracture lengths and widths. (a) Normalized fracture geometry with fracture tip width equal to 1/50 of the width at the fracture mouth. (b) Fracture transfer functions for 4.7-mm-wide fractures with varied lengths. Longer fractures have lower resonance frequencies. (c) Fracture transfer functions for 3.6-m-long fractures with varied widths. Wider fractures have higher resonance frequencies. In panels (b) and (c), dashed lines plot the quasi-static limit (equation 19).

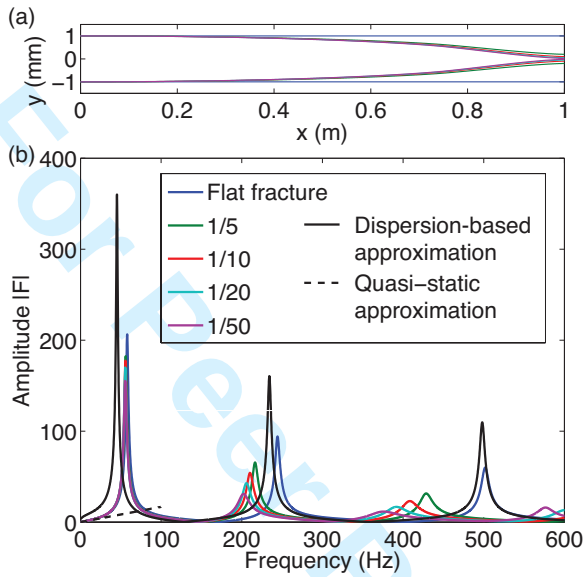


Figure 7: (a) Geometry of a 1 m long fracture with the tip width varied from 1, 1/5, 1/20, to 1/50 of the width at the fracture mouth (2 mm). (b) Amplitude of fracture transfer function with varied fracture tip width compared to the dispersion-based approximation solution (equation 20) and the quasi-static limit (equation 19).

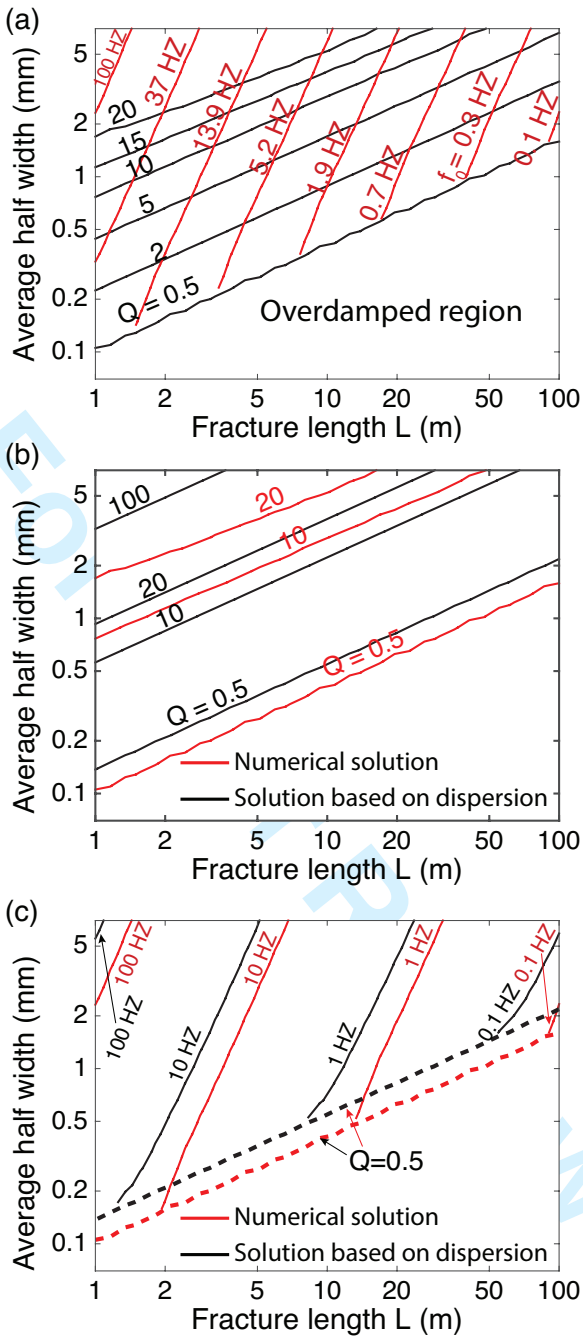


Figure 8: (a) Graphical method to determine fracture length and width from frequency (red curves) and temporal quality factor $Q$ (black curves) of the fundamental resonant mode (i.e., from the fracture transfer function from numerical simulations employing the tapered fracture geometry; see Figure 6). In the overdamped region ($Q < 0.5$) viscous dissipation prevents resonant oscillations and geometry cannot be determined with this

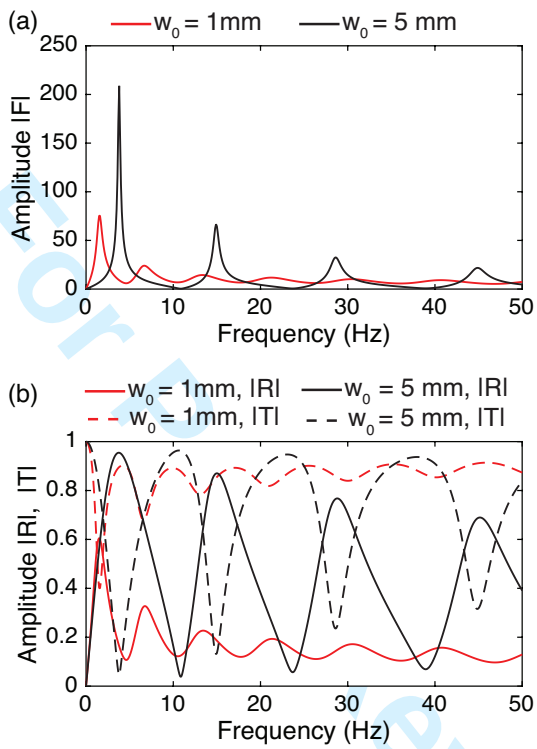


Figure 9: (a) Amplitude of fracture transfer functions, $|F|$, for two 10-m-long fractures with different widths (1 mm and 5 mm). (b) Amplitude of tube wave reflection and transmission coefficients, $|R|$ and $|T|$, across the fracture (equations 28 and 29) for wellbore diameter $2a = 0.1$ m. Maximum reflection occurs at the resonance frequencies of the fracture.

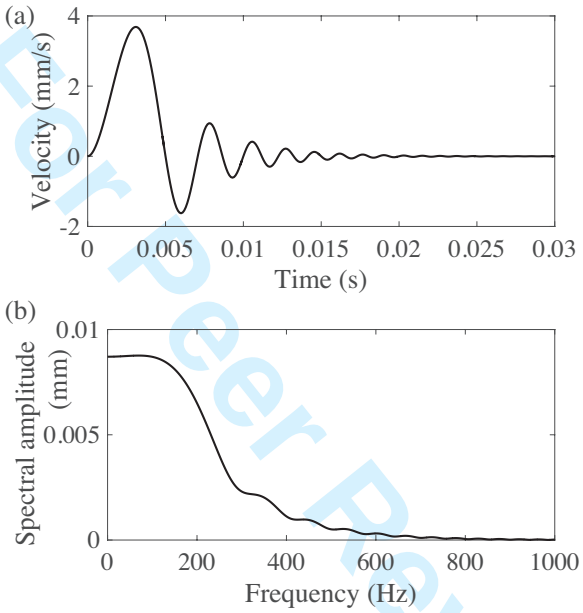


Figure 10: Chirp used for examples shown in Figures 11 and 12: (a) time series and (b) spectrum.

–

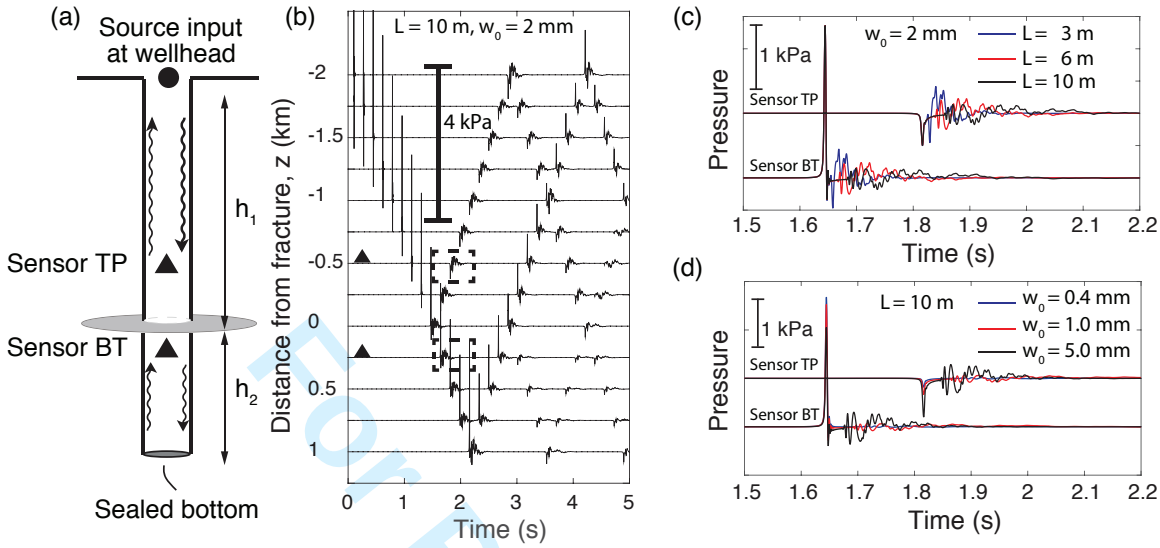


Figure 11: Response of the wellbore-fracture system to chirp excitation (Figure 10) at the wellhead. (a) Schematic of the system, with one fracture 2 km below the wellhead and 1 km above the well bottom. Sensor TP is 500 m above the fracture and sensor BT is 250 m below the fracture. (b) Record section of pressure along the wellbore (every 250 m) with a fracture that is 10 m long and 2 mm wide at the fracture mouth. Multiple reflections from the fracture, well bottom, and wellhead are observed. Dashed boxes mark the time window (1.5 s to 2.2 s) examined in (c) and (d) for sensors TP and BT. (c) Comparison of pressure at sensors TP and BT for fractures with same width but different lengths. (d) Same as (c) but for fractures with the same length but different widths. In (c) and (d), sensor TP shows waves reflected from the fracture; first arriving are direct tube wave reflections from the fracture mouth, followed by tube waves generated by Krauklis waves in the fracture that have reflected from the fracture tip. Sensor BT shows transmitted waves, which have similar arrivals. Longer fractures show a more dispersed set of Krauklis wave arrivals. Reflections are smaller from narrower fractures.

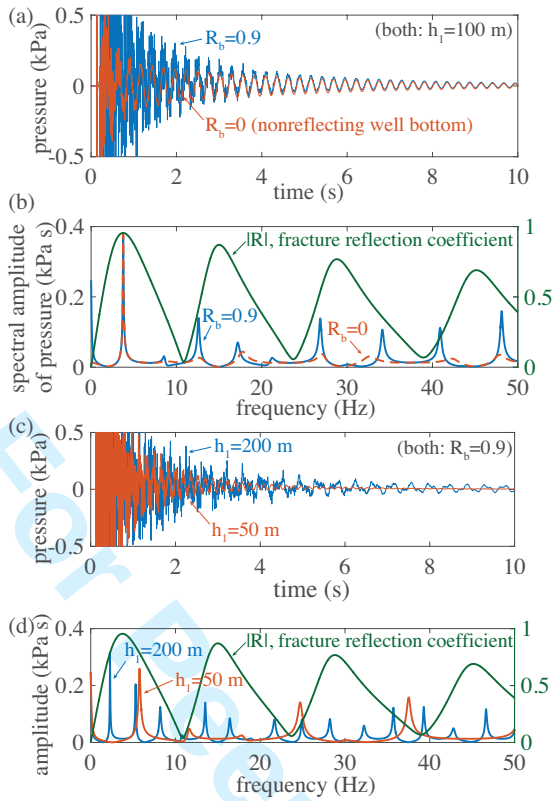


Figure 12: Matched resonance: the length of the upper wellbore section containing the source is chosen so that the resonance frequency of tube waves in this wellbore section matches the fundamental mode resonance frequency of the fracture (3.8 Hz). (a) Pressure response at a receiver in the center of the upper wellbore section (at $z = -h_1/2$) to the chirp excitation shown in Figure 10. The 3.8-Hz resonance is selectively amplified, regardless of the length of the lower wellbore section and the bottom boundary condition: compare case with nonreflecting well bottom (red, $R_b = 0$) to partially sealed (blue, $R_b = 0.9$ and $h_2 = 10$ m). (b) Fourier amplitude spectrum of pressure time series shown in (a), with prominent peak at the 3.8-Hz matched resonance frequency. While additional spectral peaks appear for the sealed bottom case, the matched resonance peak is nearly identical to the nonreflecting bottom case. Also shown is the reflection coefficient of tube waves from the fracture, which has peaks at the fracture-resonance frequencies. (c) Same as (a) but for $h_1 = 200$ m and 50 m (both with $R_b = 0.9$ and $h_2 = 10$ m). The system does not satisfy